Research Article | Open Access

Microstructures

Zhang *et al. Microstructures* **2026**, *6*, 20260133 **DOI:**10.20517/microstructures.2026.156

Deformation mechanism differences of lamellar/core-shell FCC/B2 composites: atomic simulation study

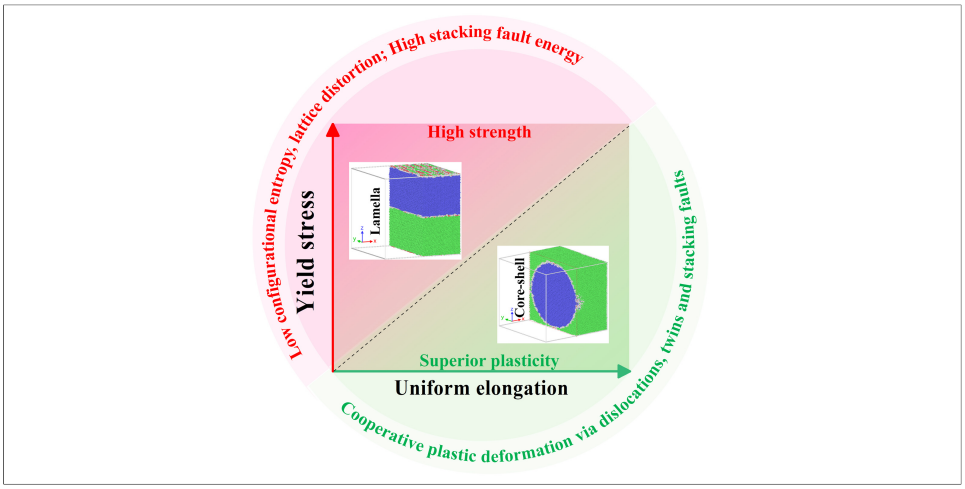
Haifeng Zhang[1,2], Nan Jia[3], Mingming Wang[1], Aiyun Zheng[1], Hongchao Ji[1,2]

Keywords:
Non-uniform structure, eutectic multi-principal element alloy, micromechanical behavior, plastic deformation mechanism, atomic simulation

Citation: Zhang, H.; Jia, N.; Wang, M.; Zheng, A.; Ji, H. Deformation mechanism differences of lamellar/core-shell FCC/B2 composites: atomic simulation study. *Microstructures* **2026**, *6*, 20260133. https://dx.doi.org/10.20517/microstructures.2026.156

Received: 24 Jun 2026 **First Decision:** 10 Jul 2026 **Revised:** 18 Jul 2026 **Accepted:** 3 Aug 2026 **Published:** 22 Oct 2026

Academic Editors: Nima Haghdadi, Yong Zhang **Copy Editor:** Ping Zhang **Production Editor:** Ping Zhang



Abstract

AlCoCrFeNi eutectic multi-principal element alloys exhibit remarkable application potential owing to their inherent heterostructures and outstanding mechanical properties. Their mechanical behaviors are governed by the synergistic deformation of non-uniformly distributed face-centered cubic (FCC) and B2 phases. Clarifying the synergistic deformation mechanisms of FCC/B2 composites is therefore essential. Herein, molecular dynamics simulations are employed to investigate the mechanical behaviors and deformation mechanisms of FCC/B2 composites with lamellar and core-shell structures in $AlCoCrFeNi_{2.1}$, $Fe_{20}Co_{20}Ni_{41}Al_{19}$ (at.%), and Ni + NiAl alloys. The results demonstrate that the elastic modulus of all composites is nearly identical during the elastic deformation stage. Upon yielding, lamellar samples display a higher yield stress yet poorer plasticity compared with the core-shell samples. The B2-core structure exhibits excellent plastic deformation capability, which originates from the coordinated activation of abundant dislocations, twins, and stacking faults suppressing void expansion. For lamellar samples, decreasing elemental diversity enhances yield strength by stabilizing heterogeneous interfaces and elevating the stacking fault energy of the FCC phase. Nevertheless, the scarcity of deformation systems promotes defect accumulation and accelerated void

Check for updates

[1]College of Mechanical Engineering, North China University of Science and Technology, Tangshan 063210, Hebei, China.
[2]Yanzhao Iron and Steel Laboratory, North China University of Science and Technology, Tangshan 063210, Hebei, China.
[3]School of Materials Science and Engineering, Northeastern University, Shenyang 110819, Liaoning, China.

Correspondence to: Dr. Haifeng Zhang, College of Mechanical Engineering, North China University of Science and Technology, Tangshan 063210, Hebei, China. E-mail: zhanghaifeng@ncst.edu.cn; Prof. Nan Jia, School of Materials Science and Engineering, Northeastern University, Shenyang 110819, Liaoning, China. E-mail: jian@atm.neu.edu.cn

growth along phase boundaries, thereby degrading the material ductility. Differently, the yield strength of the core-shell composite is less sensitive to element composition. Compared with multi-principal element alloys, pure Ni in the Ni + NiAl model exhibits higher stacking fault energy and milder lattice distortion, which hinders the activation of Shockley partial dislocations and reduces dislocation storage capacity, thereby leading to inferior plasticity. The present findings provide theoretical guidance for developing high-strength-ductility alloys with non-uniform structures.

INTRODUCTION

Non-uniform structures are prevalent in metallic materials and exert a significant influence on their mechanical behaviors[1-3]. The typical non-uniform structures include gradient structure[4,5], lamellar structure[6,7], core-shell structure[8], bimodal/multimodal structure[9], hierarchical structure[10,11], and dual/multi-phase structure[12,13], *etc.* When the intrinsic mechanical properties of different regions exhibit significant differences (> 100%), interaction between soft and hard regions under external loading triggers heterogeneous deformation, which produces a unique strengthening/toughening mechanism termed heterogeneous deformation-induced strengthening/hardening[14,15]. Extensive studies have confirmed that tailoring non-uniform structures can enable the strain hardening rate to increase continuously and remain at a high level[16-18]. Therefore, fully understanding the cooperative deformation mechanisms in heterogeneous structures is of great significance for improving strength-ductility synergy.

Eutectic Multi-Principal Element Alloys (EMPEAs) have attracted considerable attention due to the excellent castability of eutectic alloys and the excellent strength-ductility synergy of multi-principal element alloys (MPEAs)[19,20]. Among these, AlCoCrFeNi-based EMPEAs have attracted great research interest owing to their superior comprehensive mechanical properties[21-26]. The face-centered cubic ($L1_2$) [FCC($L1_2$)]/body-centered cubic (B2) [BCC(B2)] heterogeneous eutectic structure in this alloy system exhibits favorable synergistic deformation capability, endowing the alloy with high fracture strength and elevated-temperature creep resistance[22,23].

Through rational fabrication and thermomechanical processing, the FCC/B2 heterostructure can be precisely tailored to markedly improve the comprehensive mechanical performance[25-27]. For instance, after subjecting the as-cast sample to cold rolling (~85%) and annealing at ~700 °C for 1 h followed by water quenching, the $AlCoCrFeNi_{2.1}$ alloy achieves a yield strength of 1.27 GPa and a uniform elongation of 21% at room temperature[25]. Adopting this thermomechanical protocol introduces deformation twinning in $Fe_{20}Co_{20}Ni_{41}Al_{19}$ (at.%), enabling sequential multi-stage hardening throughout deformation and simultaneously boosting strength and ductility[26]. In a Ni-32.88Fe-9.53Al (wt.%) eutectic alloy, the construction of a nanoscale cocoon-like dislocation cell structure enables planar slip bands to dynamically refine the microstructure and mediate deformation transfer from FCC phase to B2 phase, promoting strength-ductility synergy[27]. Wang *et al.*[28] achieved high strength (1 GPa), high strain-hardening rate, and excellent ductility (30%) in the $Al_{0.5}Cr_{0.9}Fe_1Ni_{2.5}V_{0.2}$ alloy through grain boundary engineering. Such outstanding performance originates from the BCC/FCC ($L1_2$) core-shell structure, which mitigates stress concentrations through coordinated heterogeneous deformation and plastic strain channeling. Additionally, constructing a core-shell structure in $AlCoCrFeNi_{2.1}$ alloy via selective laser melting can also optimize the strength-ductility balance[29]. Strategies for enhancing the strength-ductility synergy of materials by tailoring heterogeneous structures have also been widely employed in various alloy systems, including ferrous alloys, copper alloys, magnesium alloys, and metallic laminate composites[30-33].

Experimental studies indicate that the grain size of EMPEAs fabricated by thermomechanical processing or laser cladding is typically at the submicron or nanometer scale[25,26,30,31,34,35]. These distinct structural morphologies correspond to markedly different deformation mechanisms[25,26,29,35]. At the nanoscale, the

cooperative deformation mechanisms and the dynamic evolutions of heterogeneous interfaces are relatively complex. In this context, molecular dynamics (MD) simulation offers unique research advantages[36-40]. Based on this method, Ji *et al.*[37] discovered that the lower stacking fault energy (SFE) of the $AlCoCrFeNi_{2.1}$ alloy favors the formation of Shockley partial dislocations (SPDs) rather than perfect dislocations in the FCC/BCC nanolayers, thereby extending the critical size for the inverse Hall-Petch relationship. Furthermore, the stress at the elastic-plastic transition point of FCC/B2 bicrystal for $AlCoCrFeNi_{2.1}$ alloy depends on the constituent single crystals. Under external loading, dislocations are more likely to nucleate at the heterogeneous interface. Instead of strengthening the material, heterogeneous interfaces tend to promote defect accumulation, leading to strain localization and non-uniform deformation of the bicrystal[38,39]. Studies on NiCoCrAl alloys indicate that their elastic modulus, yield strength, and plasticity are highly sensitive to the thickness of the FCC shell layer. If the shell thickness is less than half of the outer radius, phase transformation dominates the deformation mechanism in the BCC core region. Once the shell thickness exceeds half the particle radius, phase transformation in the core is inhibited, and overall plasticity is primarily maintained by dislocation slip in the shell[40].

Although the strength and ductility of EMPEAs can be improved by tailoring the morphology of heterogeneous structures (lamellar/core-shell), the following scientific questions remain unresolved. (1) The differences in mechanical behaviors of EMPEAs with lamellar and core-shell structures are unclear; (2) The physical mechanisms that govern mechanical responses remain uncertain; (3) It remains unknown whether the characteristics of mechanical behaviors and deformation mechanisms for lamellar and core-shell structures are universally applicable to other metallic materials. These gaps limit our understanding of the synergistic deformation mechanisms across diverse non-uniform structures and hinder further improvements of strength and ductility.

To address these scientific issues, this work takes the FCC/B2 composite widely existing in AlCoCrFeNi EMPEAs as the research object. The mechanical behavior of metallic materials is closely related to the activation of microscopic deformation systems. The size of dislocation nucleation at the early stage is usually in the nanoscale. Therefore, tracking the evolution of deformation systems at the nanoscale is particularly important for a deeper understanding of the mechanical behavior. A large number of research findings indicate that the evolution of deformation mechanisms at the nanoscale based on MD simulation methods can be consistent with experiments[36-39]. Therefore, MD simulations were used to study the micromechanical behaviors and synergistic deformation mechanisms of multiple deformation modes for FCC/B2 composites with lamellar and core-shell structures in $AlCoCrFeNi_{2.1}$, $Fe_{20}Co_{20}Ni_{41}Al_{19}$ (at.%), and Ni + NiAl alloys under uniaxial tensile deformation. The influence of structural heterogeneity on mechanical behaviors and the underlying physical mechanisms is systematically revealed. Furthermore, by examining the deformation processes of composites with different compositions, the effects of configuration entropy on micro-deformation mechanisms were elucidated. The findings provide theoretical guidance for the design of high-strength and high-ductility alloys containing non-uniform structures.

MODELS AND METHODS

Simulation models

In this work, the mechanical behaviors and cooperative deformation mechanisms for FCC/B2 composites with lamellar and core-shell structures in $AlCoCrFeNi_{2.1}$, $Fe_{20}Co_{20}Ni_{41}Al_{19,}$ and Ni + NiAl alloys were studied. Furthermore, the universality of the relevant deformation mechanisms was explored by comparing the composites with different configurational entropies. Experimental studies show that the compositions of the FCC and B2 phases in the $AlCoCrFeNi_{2.1}$ alloy are $Al_{9.04}Co_{19.41}Cr_{20.77}Fe_{18.53}Ni_{32.23}$ and $Al_{27.56}Co_{13.24}Cr_{5.55}Fe_{10.21}Ni_{43.42}$ (at.%), respectively (All alloy compositions studied in this paper are in atomic percent except $AlCoCrFeNi_{2.1}$ and Ni + NiAl)[34]. According to the energy dispersive spectroscopy results obtained from the B2 and

FCC phase microregions of the FeCoNiAl alloy after approximately 83% cold rolling and short-time annealing at 660 °C, the compositions of the FCC phase and BCC phase are roughly $Fe_{27}Ni_{41}Co_{27}Al_5$ and $Fe_{19}Ni_{43}Co_{19}Al_{19}$, respectively[26]. These values do not represent the overall alloy composition. To match experimental measurements, the FCC-phase compositions of the two alloys were set as $Al_{9.04}Co_{19.41}Cr_{20.77}Fe_{18.53}Ni_{32.23}$ and $Fe_{27}Ni_{41}Co_{27}Al_5$. In the Ni + NiAl model, the FCC phase was pure Ni. To simplify the ordered B2 phase, the B2 phase composition was uniformly set to NiAl. The primary contributing factors are summarized as follows. First, Fe, Co, and Cr exhibit low contents in the B2 phase of the two eutectic high entropy alloys (EHEAs)[26,34]. Second, inadequate experimental evidence for the atomic site occupation of these elements prevents accurate atomic-scale modeling of the B2 phase. Third, this study mainly investigates the coordinated deformation mechanisms of the FCC/B2 composite. Although the B2 phase is simplified to pure NiAl, dislocation slip remains the dominant deformation mechanism in the B2 phase. This is consistent with experimental investigations on $AlCoCrFeNi_{2.1}$ and $Fe_{20}Co_{20}Ni_{41}Al_{19}$ (at.%) alloys[25,26]. Accordingly, the B2-phase composition was temporarily simplified to NiAl.

To reveal the influence of phase distribution variations in core-shell structures on mechanical behavior, B2-core/(FCC-shell) and FCC-core/(B2-shell) models were also constructed for comparison. The atomic and dislocation structures of the different structural models represented by the $AlCoCrFeNi_{2.1}$ alloy are shown in Figure 1. Compared with the lamellar model, core-shell models contain more unknown atoms at the heterogeneous interface, indicating a rougher interface structure. Dislocation analysis reveals a small number of dislocations at the heterogeneous interfaces of each model. Only the FCC phase was varied to introduce entropy differences, while the B2-phase composition remained unchanged. The dimensions of all models are 20(X) × 20(Y) × 20(Z) nm^3. The core region in the core-shell structure model is spherical. The volume fraction ratio of FCC to B2 phase in all models is fixed at V_{FCC}:V_{B2} = 1:1, with a total number of atoms ranging from 675,000 to 695,000. The diameter of the core sphere calculated from the volume is slightly smaller than the total length of the model. Therefore, adjacent core structures appear relatively close to each other under periodic boundary conditions. Studies have shown that the FCC and B2 phases in EHEAs follow the K-S orientation relationship, namely $(11\bar{2})_{FCC}//(11\bar{2})_{B2}$, $(\bar{1}10)_{FCC}//(111)_{B2}$ and $(111)_{FCC}//(\bar{1}10)_{B2}$ [35,36,41]. Therefore, the crystal orientations of FCC and B2 along the X, Y, and Z directions are $[11\bar{2}]$, $[\bar{1}10]$, [111] and $[11\bar{2}]$, [111], $[\bar{1}10]$, respectively. Uniaxial tensile deformation simulations were performed along the Z-direction.

MD simulations and analyses

The atomic-scale simulations in this work were performed using the large-scale atomic/molecular massively parallel simulator (LAMMPS) software[42]. The embedded atom method (EAM) potential function developed by Farkas *et al.*[43] was used to describe the interactions between different atoms. Based on this potential, the calculated lattice parameter and single-crystal elastic constants (C_{11}, C_{12}, C_{44}) of B2-phase NiAl are 0.3 nm, 183.7, 112.6, and 93.3 GPa, respectively. For the FCC phase in $AlCoCrFeNi_{2.1}$, the corresponding lattice parameter and elastic constants (C_{11}, C_{12}, C_{44}) are 0.359 nm, 255, 213, and 173 GPa. All these calculated results exhibit good consistency with experimental measurements[24]. Besides, the EAM potential has been widely used to study the mechanical behaviors and micro-deformation mechanisms of AlCoCrFeNi alloys[44-47]. The time step was 5 fs. Before deformation, each model was first fully relaxed in an isobaric-isothermal ensemble to reach an equilibrium state at 300 K. A periodic boundary condition was applied along the three orthogonal directions. Previous MD studies on FCC and B2 structured alloy models have shown that strain rates ranging from 10^7 to 10^9 s^{-1} generate no significant effect on the deformation mechanism[39,48]. To improve computational efficiency, the strain rate was set to 10^8 s^{-1}. The total engineering strain was set to 50% in order to obtain the evolution laws of different deformation systems under large plastic deformation. Simulation results were visualized using the Open Visualization Tool

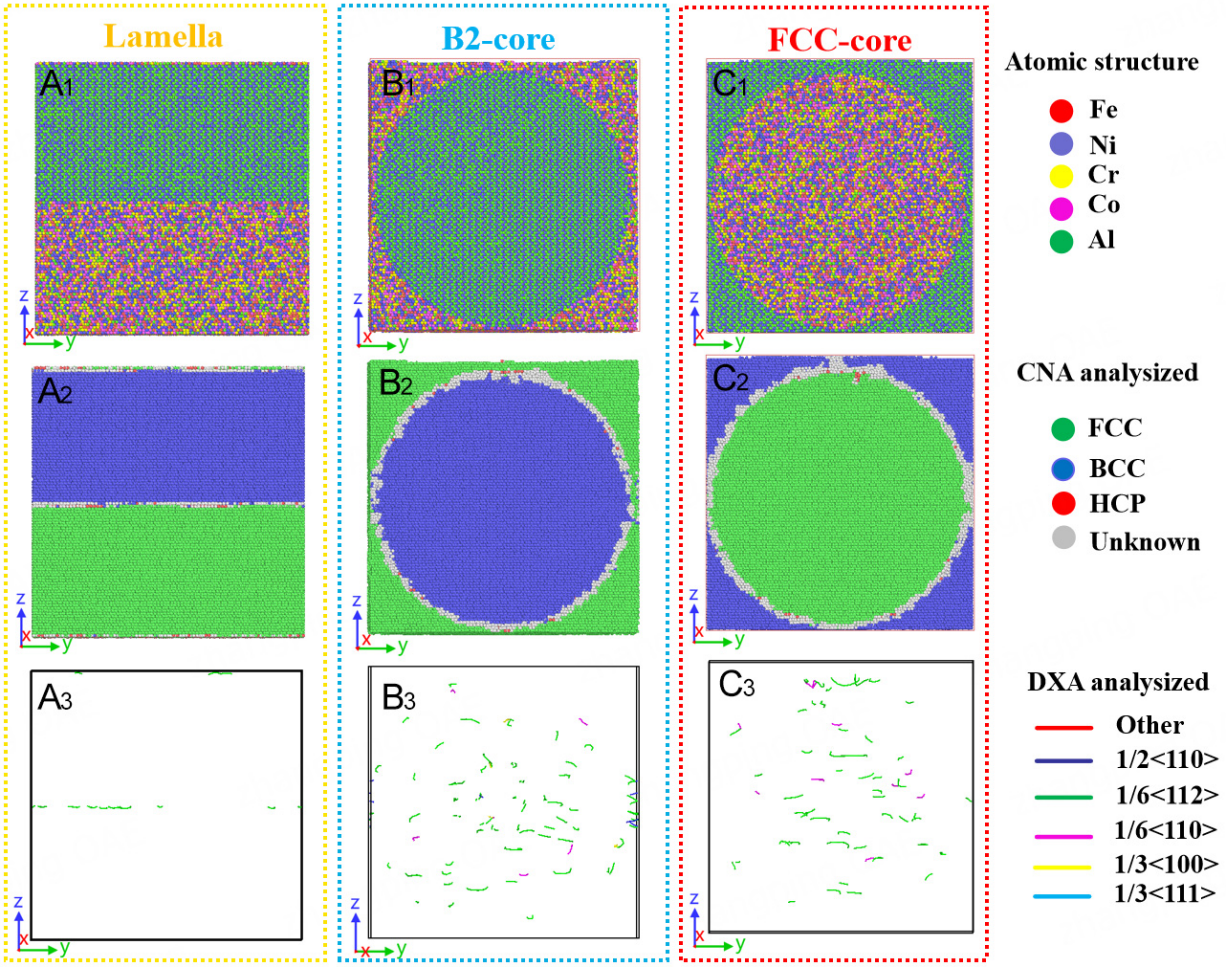


Figure 1. Atomic and dislocation structures of the $AlCoCrFeNi_{2.1}$ alloy models with lamellar and core-shell structures after mid-sectioning along the X-direction. (A_1-A_3), (B_1-B_3), and (C_1-C_3) correspond to lamella, B2-core, and FCC-core structures, respectively. (A_2-C_2) and (A_3-C_3) represent the atomic structures characterized by CNA and the dislocation structures identified by DXA, respectively. FCC: Face-centered cubic; BCC: body-centered cubic; HCP: hexagonal close-packed; CNA: common neighbor analysis; DXA: dislocation analysis.

software[49]. Dislocation types and atomic structures were analyzed using the dislocation analysis (DXA)[50] and common neighbor analysis (CNA)[51], respectively. The voids were quantitatively analyzed using the Gaussian density method built into the Construct Surface Mesh modifier[52].

RESULTS

Mechanical behaviors

The stress-strain curves of three metal models with different non-uniform structures, as well as the strain values at different deformation stages, are shown in Figure 2. The whole deformation process was divided into four stages: elastic deformation stage, work-hardening stage (flow stress > 4 GPa), stress-stabilized stage (2.5 GPa < flow stress < 4 GPa), and fracture stage (flow stress < 2.5 GPa). For all models, stress increases approximately linearly with increasing strain during the elastic deformation stage, and the slopes of all stress-strain curves are nearly identical, indicating similar elastic moduli. At the elastic-plastic transition point (maximum stress also defined as the yield stress), the lamellar structure in all three alloy systems exhibits a significantly higher yield stress and corresponding yield strain than the core-shell structure [Figure 2A_2-C_2]. This result is consistent with experimental observations that the yield stress of lamella-structured $AlCoCrFeNi_{2.1}$ is higher than that of its core-shell structure[25,29]. The yield stress of the lamellar model increases with decreasing elemental species, whereas that of the core-shell model is less sensitive to the number of alloying elements. For metal models with identical composition, yield strength varies among different core-shell structures. For the FCC-core models of $AlCoCrFeNi_{2.1}$ and $Fe_{20}Co_{20}Ni_{41}Al_{19}$ alloys, the

yield stress is higher than that of the B2-core models, whereas the opposite trend is observed in the Ni + NiAl model.

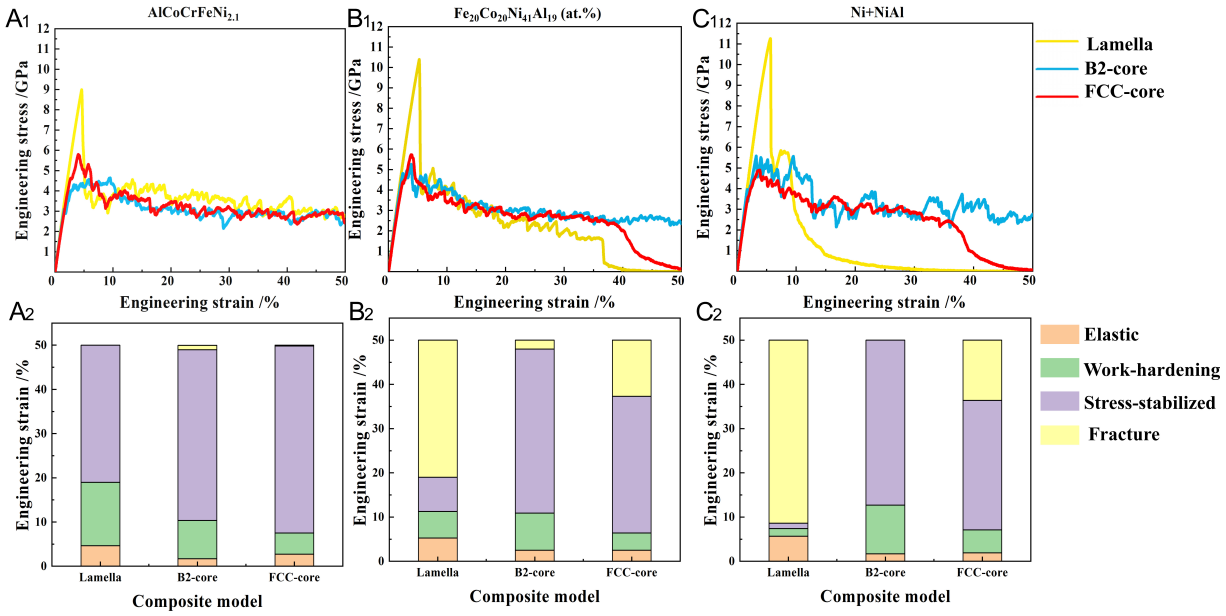


Figure 2. (A_1-C_1) Stress-strain curves of three metallic models with different non-uniform structures and (A_2-C_2) the corresponding strain values at different deformation stages. FCC: Face-centered cubic.

After yielding, the stress of lamellar models decreases rapidly with increasing strain, then rebounds noticeably after reaching a minimum. For core-shell models, stress also fluctuates with increasing strain but with milder amplitude and maintains a high flow stress (> 4 GPa) [Figure 2A_1-C_1]. This regime is defined as the work-hardening stage due to pronounced work hardening in all models. During this stage, the corresponding strains in the $AlCoCrFeNi_{2.1}$ alloy models follow the order: lamella > B2-core > FCC-core. In the $Fe_{20}Co_{20}Ni_{41}Al_{19}$ models, the FCC-core model exhibits the smallest strain. For Ni + NiAl, the B2-core model exhibits the largest strain, followed by the FCC-core, and the lamella has the smallest strain. With decreasing element species, the strains of the work-hardening stage decrease significantly in lamellar models but show no obvious change in core-shell models [Figure 2A_2-C_2].

With further deformation, the flow stress of the lamellar Ni + NiAl model decreases rapidly to zero. However, the flow stresses for the other models slowly stabilize above 2.5 GPa at relatively large strains. Meanwhile, stress fluctuation amplitude diminishes with increasing strain [Figure 2A_1-C_1]. This regime is designated the stress-stabilization stage. During this stage, the strain of lamellar models decreases with reducing element species, and core-shell models display larger strains than lamellar models. Among all models, the lamellar Ni + NiAl model exhibits the lowest strain [Figure 2C_2]. This indicates that at the nanoscale, the plastic deformation capability of the lamellar structure decreases with the reducing element species, whereas the core-shell structure maintains favorable plastic deformation capability. In the late deformation stage (fracture stage), the lamellar $Fe_{20}Co_{20}Ni_{41}Al_{19}$ model, as well as the lamellar and FCC-core Ni + NiAl models, exhibit a sharp drop in stress compared with other models, indicating poor uniform deformation capability.

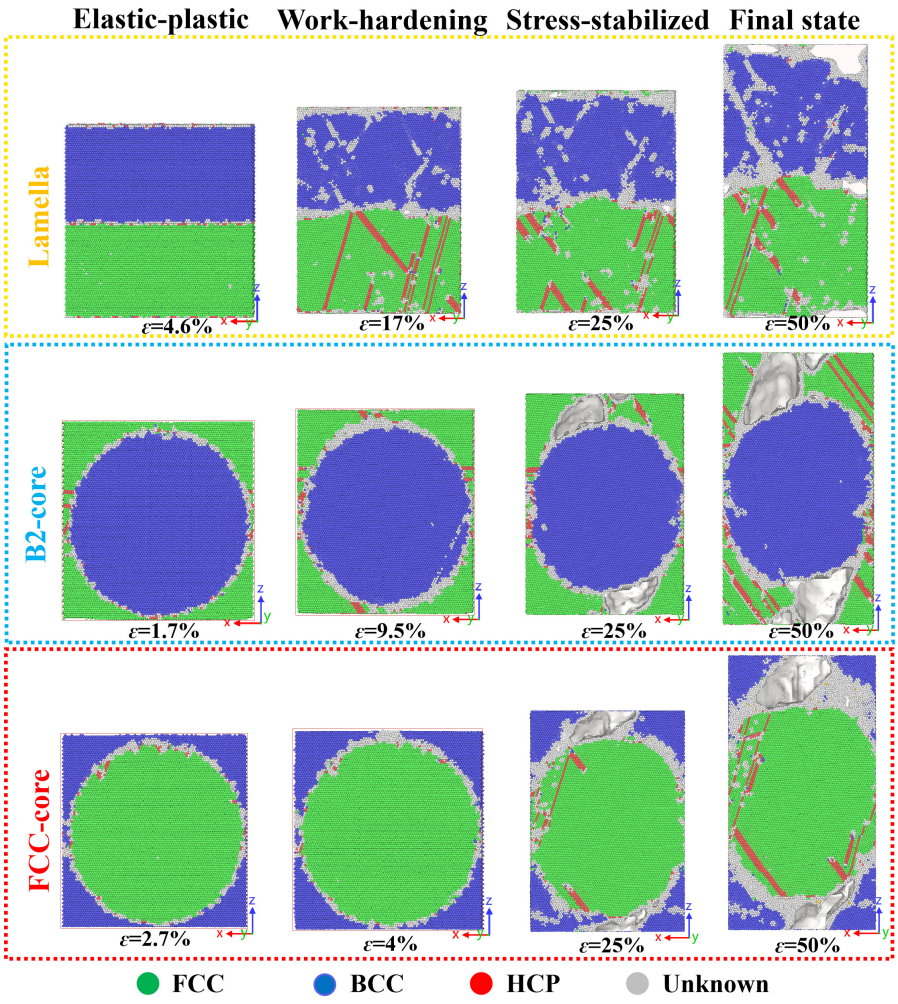


Figure 3. Characteristic atomic structures of $AlCoCrFeNi_{2.1}$ models with different structures at various strain stages. The irregular off-white regions correspond to voids generated during tensile deformation. FCC: Face-centered cubic; BCC: body-centered cubic; HCP: hexagonal close-packed.

Microstructures and deformation systems evolution

$AlCoCrFeNi_{2.1}$

To reveal the physical mechanisms underlying the distinct mechanical behaviors, the characteristic atomic structures of the $AlCoCrFeNi_{2.1}$ alloy with different structural models are shown in Figure 3. At the elastic-to-plastic transition point, a small number of hexagonal close-packed (HCP) atoms appear at heterogeneous interfaces, indicating that dislocations begin to nucleate at the phase boundaries of all three structural models. During the work-hardening stage, numerous deformation systems are activated in both FCC and B2 phases of the lamellar model. Specifically, within the FCC phase, stacking faults and twin boundaries are formed via SPD slip. In the B2 phase, atoms associated with post-slip deformation systems are identified as unknown atoms[38,39,53]. The heterogeneous interface in the lamellar structure evolves from a flat state before deformation to a curved state bent toward the B2 phase. The number of activated deformation systems in core-shell models is noticeably lower than that in the lamellar model. During the stress-stabilized stage, the deformation systems in all three models further increase, and voids induced by defect concentration appear at the heterogeneous interfaces in all models, among which the voids in the core-shell structures are relatively significant. Under continued loading, the propagation of these voids leads to fracture of all models.

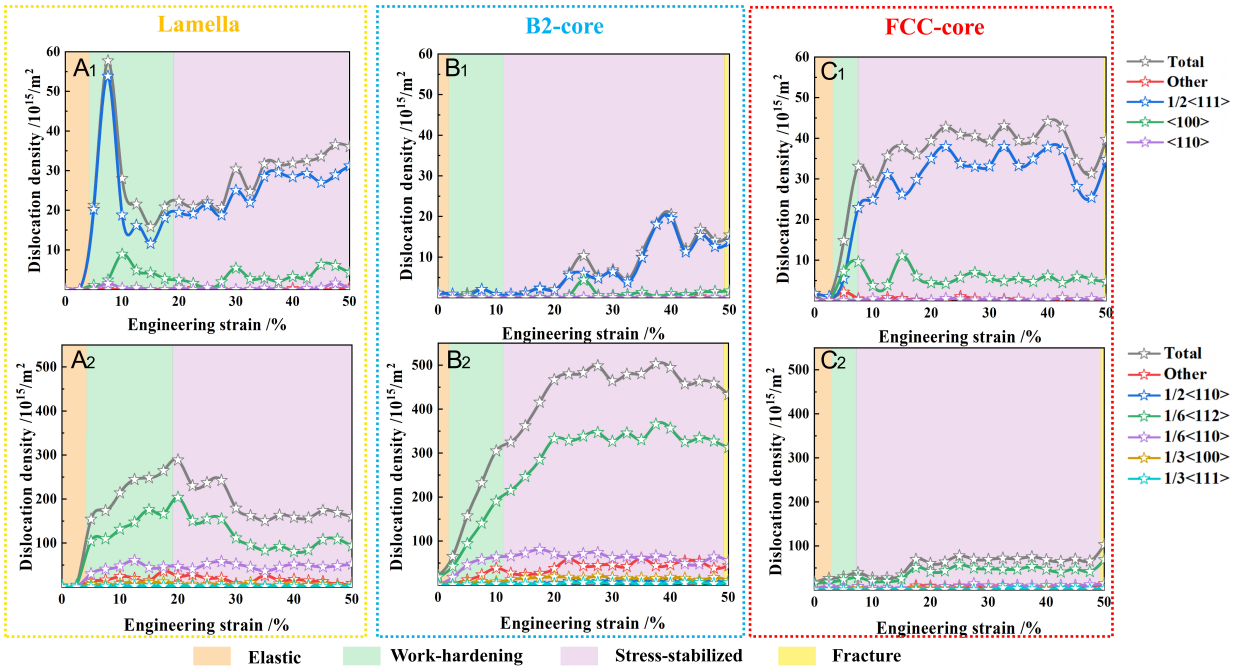


Figure 4. Evolutions of dislocation densities in the (A_1-C_1) B2 phase and (A_2-C_2) FCC phase during deformation for $AlCoCrFeNi_{2.1}$ models with different structures. FCC: Face-centered cubic.

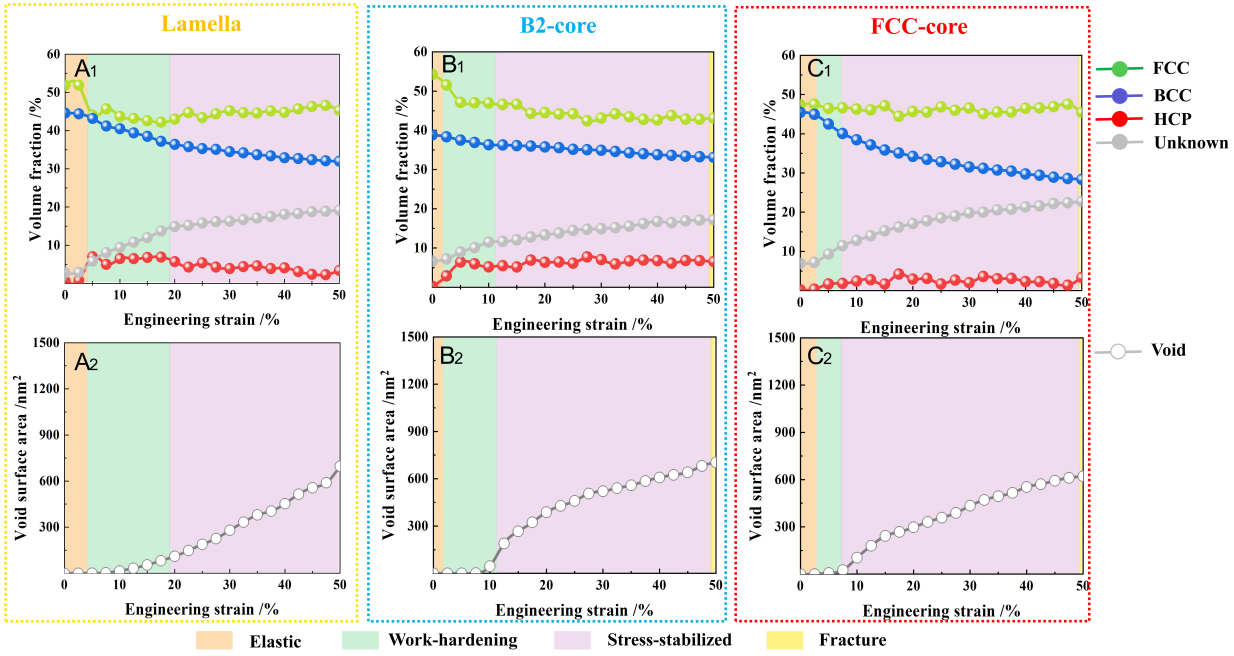


Figure 5. Evolutions of (A_1-C_1) atomic volume fraction of different phases and (A_2-C_2) void surface area for $AlCoCrFeNi_{2.1}$ models with different structures. FCC: Face-centered cubic; BCC: body-centered cubic; HCP: hexagonal close-packed.

In MD simulations of the plastic deformation process for metallic materials, stress fluctuations are closely related to the activation and evolution of deformation systems, such as dislocation slip, twinning, phase transitions, and voids[38,39,41]. Therefore, the evolutions of dislocation density (DD), phase volume fraction (PVF), and void surface area (VSA) during uniaxial tension were analyzed quantitatively. The DD evolutions in B2 and FCC phases for different structural models are shown in Figure 4, while the evolutions of the PVF and the VSA are presented in Figure 5.

During the elastic deformation stage, no obvious dislocation activity is observed in all models, and PVFs remain consistent with the initial state [Figure 4A$_1$ and A$_2$, Figure 5A$_1$]. During the work-hardening stage, the dislocation densities in both B2 and FCC phases of the lamellar model increase sharply, causing a rapid stress drop [Figure 2A$_1$]. The dominant dislocation types in FCC and B2 phases are 1/6<112> SPD and 1/2<111> dislocation, respectively. In the present study, the dominant deformation systems of FCC are SPDs and stacking faults, rather than perfect dislocations. This is mainly attributed to the small grain size and high strain rate of the model employed in MD simulations, which enables the activation of partial dislocations and stacking faults that are difficult to trigger in experiments. In Figure 4A$_1$, the dislocation density in the B2 phase increases first and then decreases. The decrease in dislocation density is mainly attributed to the increase in the number of unknown atoms and the growth of void volume [Figure 5A$_1$ and A$_2$]. In the B2-core model, the DD in the FCC phase increases significantly, whereas no obvious dislocation activation occurs in the B2 phase [Figure 4B$_1$ and B$_2$]. In contrast, dislocation slip is activated in both phases within the FCC-core structure [Figure 4C$_1$ and C$_2$]. Due to dislocation activation, a small number of FCC and BCC atoms transform into unknown atoms. In the FCC phase, the formation of stacking faults and twins transforms FCC atoms into HCP atoms [Figure 5A$_1$-C$_1$]. In the lamellar model, a small number of voids are also formed due to dislocation accumulation at the heterogeneous interfaces [Figure 5A$_2$]. The activation and slip of dislocations dominate deformation during this deformation stage.

In the stress-stabilized stage, the DD in the B2 phase of the lamellar model increases gradually with increasing strain, while that in the FCC phase gradually decreases and then stabilizes [Figure 4A$_1$ and A$_2$]. In core-shell models, the DD in each phase increases gradually and then stabilizes [Figure 4B$_1$, B$_2$, C$_1$ and C$_2$]. Meanwhile, as the volume fractions of FCC and BCC gradually decrease, the number of unknown atoms gradually increases, but the rate of change gradually decreases with increasing strain. However, the VSA increases significantly in each model, indicating that void growth dominates the late-stage deformation and is the main factor leading to fracture [Figure 5]. Notably, during the entire deformation process, more dislocations are activated in the FCC phase than in the B2 phase for all models. In the core-shell structure, the same phase activates significantly fewer dislocations when serving as the core than as the shell [Figure 4]. Notably, the dislocation densities in FCC/B2 composites are relatively larger compared with experimental results. According to experimental studies, transmission electron microscopy is usually used to observe dislocations in thin samples, including nano-pillars, but may underestimate the dislocation density because of the invisibility criterion for diffraction contrast imaging. However, the length of dislocations can be calculated accurately by the DXA[50], thus, the dislocation densities in simulations are higher than experimental results.

$Fe_{20}Co_{20}Ni_{41}Al_{19}$

The characteristic atomic structures of the $Fe_{20}Co_{20}Ni_{41}Al_{19}$ alloy with different structural models are displayed in Figure 6. At the elastic-to-plastic transition point, dislocations are activated only within the FCC phase in the lamellar model, accompanied by stacking fault formation via dislocation slip. During the work-hardening stage, more deformation systems are activated in the lamellar model than in core-shell models. With increasing strain, deformation systems within each model intensify, and obvious voids are formed at the heterogeneous interfaces. Subsequently, void growth leads to fracture. Compared with the $AlCoCrFeNi_{2.1}$ alloy, void expansion in the lamellar model for the $Fe_{20}Co_{20}Ni_{41}Al_{19}$ alloy is more rapid, making it more prone to early fracture.

The evolutions of DD in B2 and FCC phases, PVF, and the VSA are shown in Figures 7 and 8, respectively. Dislocations are activated in all models after yielding, and DD increases rapidly with increasing strain. However, in core-shell models, the DD in the core phase shows no obvious change, indicating that plastic deformation occurs mainly in the shell during the early deformation stage [Figure 7]. Dislocation activation

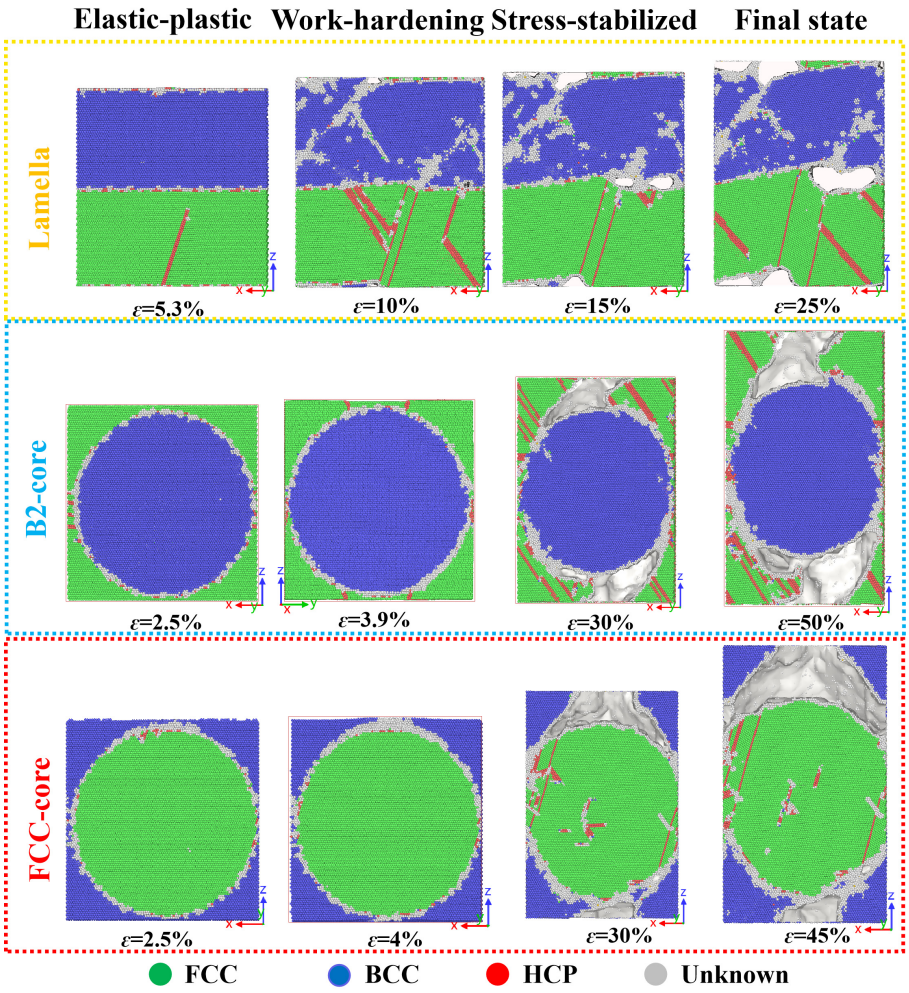


Figure 6. Characteristic atomic structures of $Fe_{20}Co_{20}Ni_{41}Al_{19}$ models with different structures at various strain stages. The irregular off-white regions correspond to voids generated during tensile deformation. FCC: Face-centered cubic; BCC: body-centered cubic; HCP: hexagonal close-packed.

induces stacking faults in the FCC phase, converting a small number of FCC atoms to HCP atoms. Concurrently, increasing defects transform some FCC and BCC atoms into unknown atoms. In the lamellar model, defect accumulation at heterogeneous interfaces generates voids and increases VSA [Figure 8]. During the stress-stabilized stage, the core of the core-shell model undergoes plastic deformation, raising DD. The DD in all models reaches its maximum level [Figure 7]. The continuous activation of dislocations leads to the transformation of FCC and BCC atoms into HCP and unknown atoms [Figure 8A_1-C_1]. Meanwhile, the voids in each model propagate rapidly and gradually dominate the plastic deformation until fracture occurs [Figure 8A_2-C_2]. Throughout the whole plastic deformation, more dislocations are activated in the FCC phase than in the B2 phase. In the core-shell models, the same phase activates fewer dislocations when acting as the core than as the shell [Figure 7].

Ni + NiAl

The atomic structures of Ni + NiAl with different structural models are shown in Figure 9. No deformation systems are activated in any model at the elastic-plastic transition point. During the work-hardening stage, in the lamellar model, stacking faults are activated in the FCC phase. However, predominant dislocation slip occurs in the B2 phase, followed by rapid fracture, leading to degraded plastic deformability. In core-shell models, dislocation slip occurs in both the FCC and B2 phases. Unknown atoms generated by dislocation

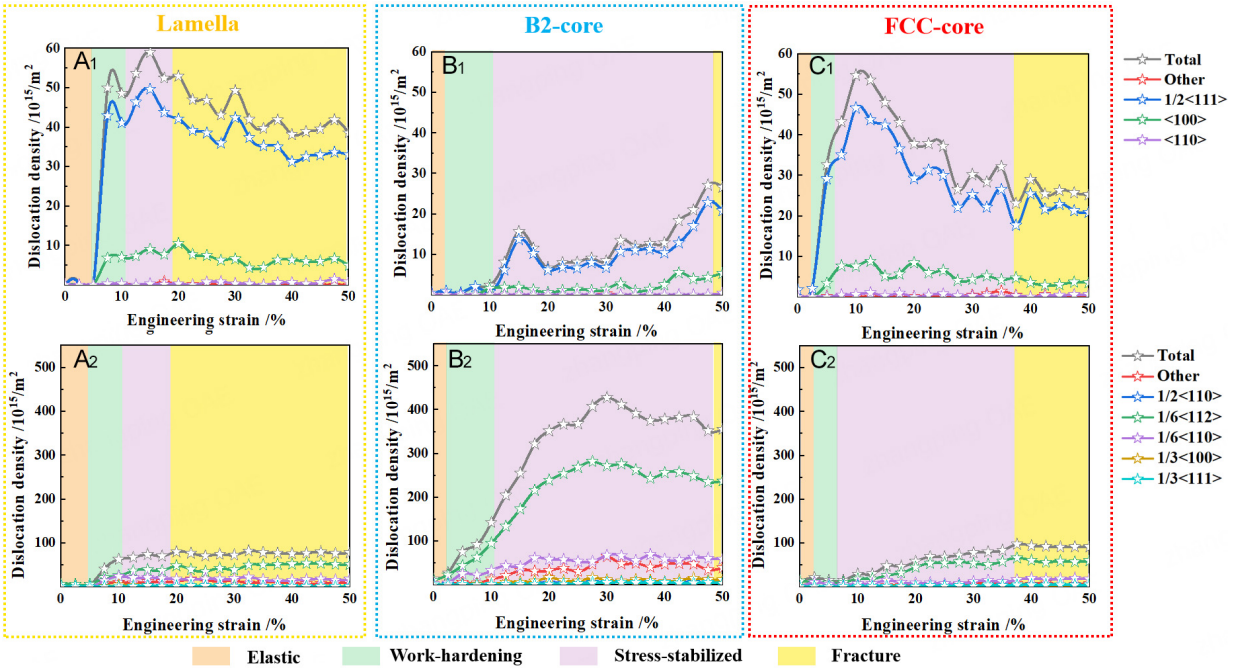


Figure 7. Evolutions of dislocation densities in the (A_1-C_1) B2 phase and (A_2-C_2) FCC phase during deformation for $Fe_{20}Co_{20}Ni_{41}Al_{19}$ models with different structures. FCC: Face-centered cubic.

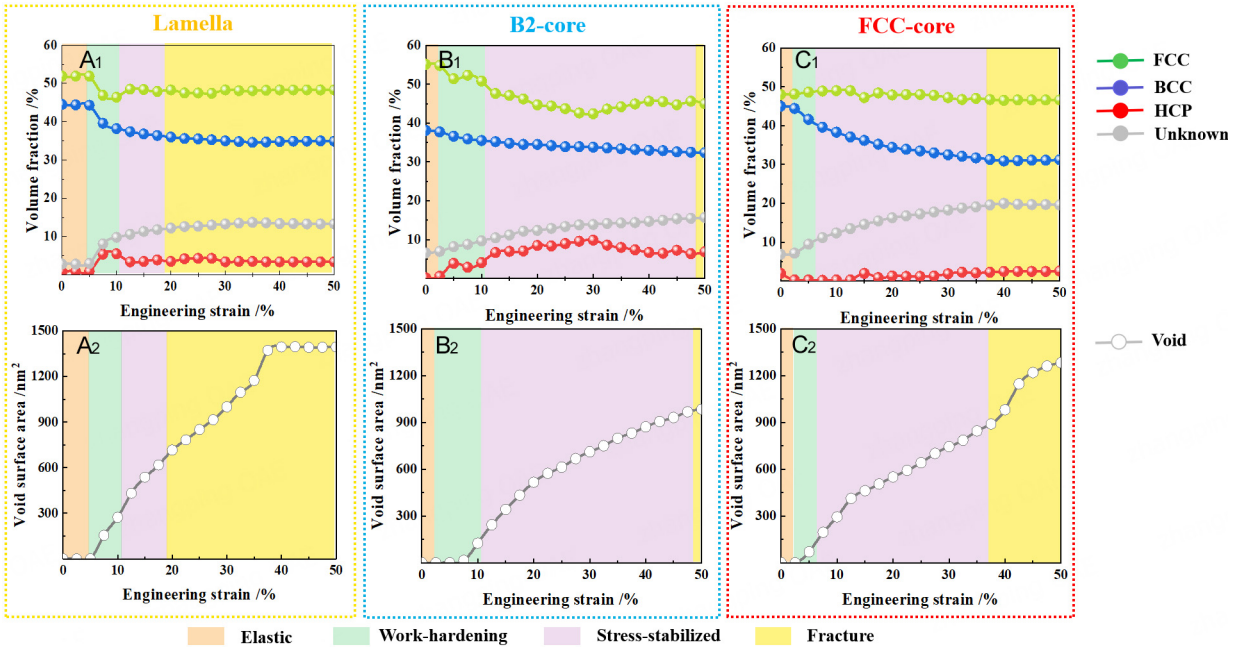


Figure 8. Evolutions of (A_1-C_1) atomic volume fraction of different phases and (A_2-C_2) void surface area for $Fe_{20}Co_{20}Ni_{41}Al_{19}$ models with different structures. FCC: Face-centered cubic; BCC: body-centered cubic; HCP: hexagonal close-packed.

slip are observed in the B2 phase, while no obvious void is formed. With increasing strain, stacking faults and twins are activated in the FCC phase of the core-shell models, and voids are formed at the heterogeneous interfaces during the stress-stabilized stage. Subsequently, void propagation leads to model fracture. Notably, no dislocation accumulation at heterogeneous interfaces or corresponding back-stress hardening occurs during plastic deformation in any model. Based on the dislocation pile-up theory, the critical width of the

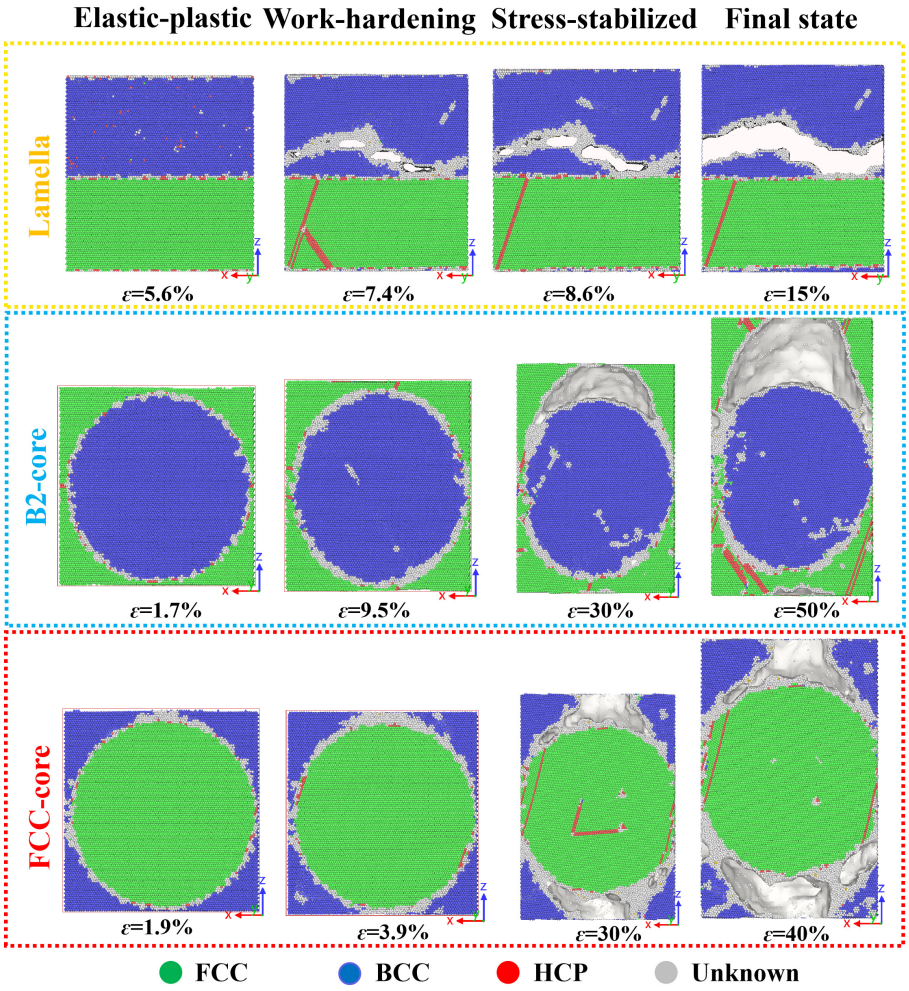


Figure 9. Characteristic atomic structures of Ni + NiAl models with different structures at various strain stages. The irregular off-white regions correspond to voids generated during tensile deformation. FCC: Face-centered cubic; BCC: body-centered cubic; HCP: hexagonal close-packed.

hetero-boundary-affected zone is approximated as 33 nm[37,54]. However, the model size in this work is significantly smaller than the critical size. The crystals lack sufficient space to accommodate dislocation pile-up, so no back-stress hardening is generated.

The evolutions of DD in the B2 and FCC phases, PVF, and the VSA for Ni + NiAl models are shown in Figures 10 and 11, respectively. For the elastic deformation stage, no obvious deformation systems are activated in all models. As a result, the DD, PVF, and VSA remain unchanged. During the work-hardening stage, dislocation slip is considerably more active in the B2 phase than in the FCC phase for the lamellar model. This results in a decrease in the volume fraction of BCC phase atoms and an increase in the volume fraction of unknown atoms [Figure 10A$_1$ and 11A$_1$]. In addition, the VSA increases rapidly [Figure 11A$_2$], which is the main reason for fracture at a strain less than 10%. In the core-shell models, dislocation slip occurs in both phases. Specifically, the DD of the FCC phase in the B2-core model is significantly higher than that of the B2 phase, whereas the opposite trend is observed in the FCC-core model [Figure 10]. Dislocation activation reduces the volume fractions of BCC and FCC atoms and increases the volume fractions of HCP and unknown atoms. The surface area of the voids in core-shell models does not increase significantly [Figure 11]. Owing to rapid void propagation and early fracture, the lamellar model quickly enters the fracture stage with no further changes in deformation systems. However, the DD in the core-shell models

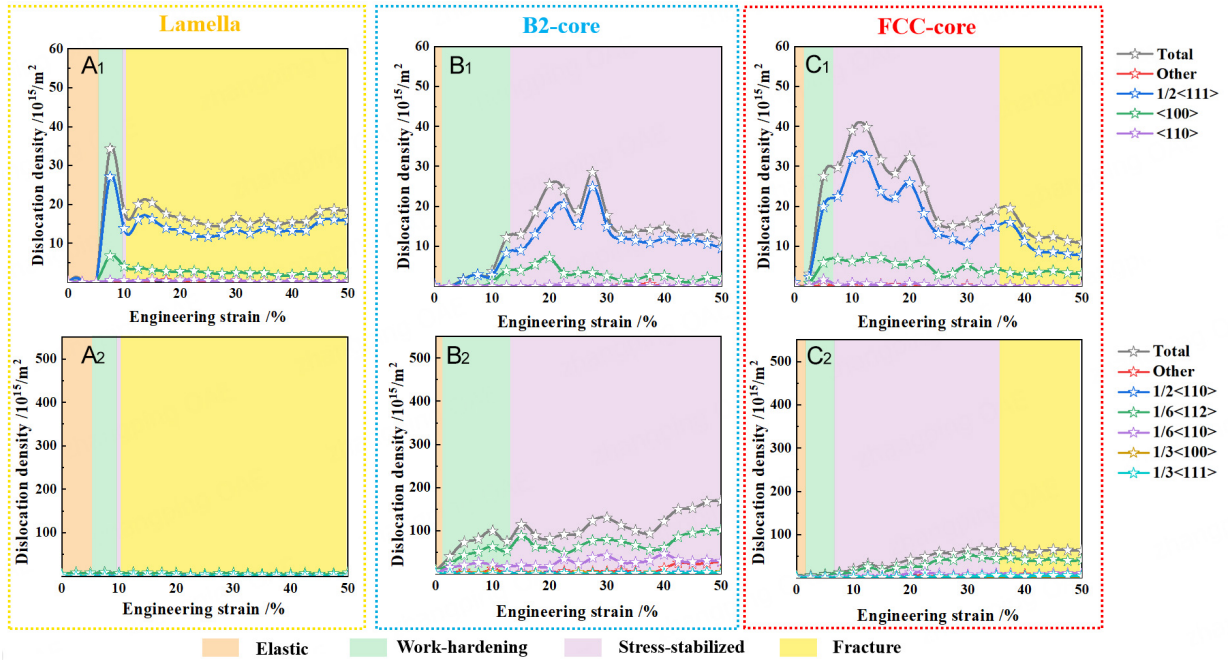


Figure 10. Evolutions of dislocation densities in the (A_1-C_1) B2 phase and (A_2-C_2) FCC phase during deformation for Ni + NiAl models with different structures. FCC: Face-centered cubic.

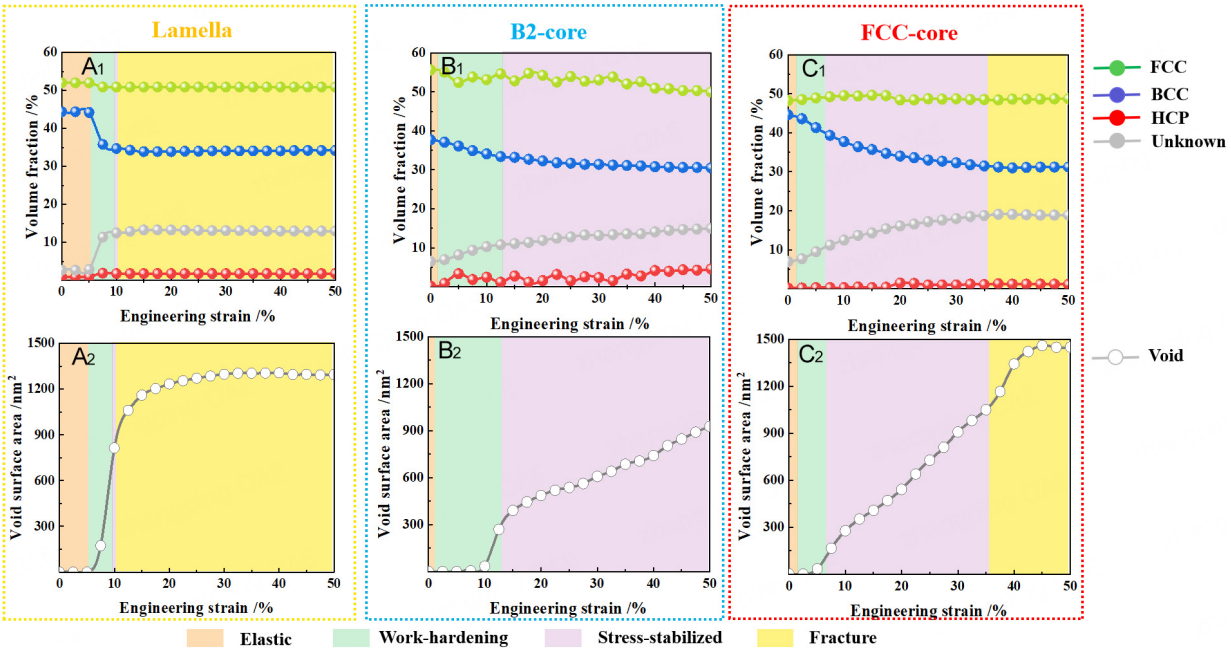


Figure 11. Evolution of (A_1-C_1) atomic volume fraction of different phases and (A_2-C_2) void surface area for Ni + NiAl models with different structures. FCC: Face-centered cubic; BCC: body-centered cubic; HCP: hexagonal close-packed.

fluctuates to varying degrees during the stress-stabilized stage. More dislocations are activated in the FCC phase for the B2-core model, resulting in an increase in the volume fraction of HCP phase atoms. Since more dislocations are activated in the B2 phase for the FCC-core model than in the B2-core model, the volume fraction of unknown atoms increases more significantly [Figures 10B_1, C_1, B_2, C_2 and 11B_1, C_1]. During this stage, the VSA in core-shell models increases rapidly and gradually dominates the subsequent deformation. With further loading, void propagation causes model fracture. Notably, during the plastic deformation stage, for models with the same structure but different compositions, the density of activated dislocations in the FCC phase decreases with decreasing alloying element species [Figures 4, 7 and 10].

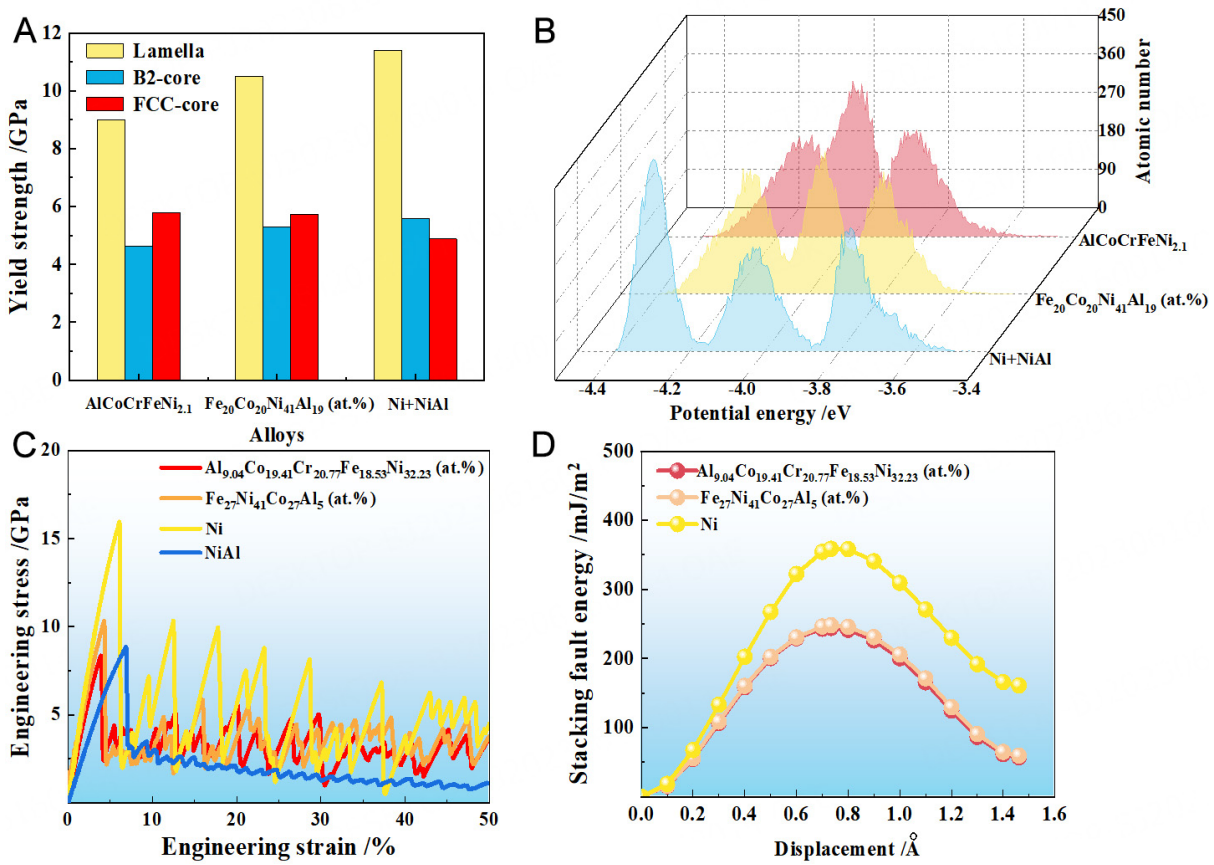


Figure 12. (A) Yield strength of three metallic models with different non-uniform structures; (B) Atomic potential energy analysis at heterogeneous interfaces in lamella models with different compositions; (C) Engineering stress-strain curves of FCC single crystals ($Al_{9.04}Co_{19.41}Cr_{20.77}Fe_{18.53}Ni_{32.23}$, $Fe_{27}Ni_{41}Co_{27}Al_5$ and pure Ni) under uniaxial tension along the [111] direction, and of B2 single crystal (NiAl) under uniaxial tension along the [110] direction; (D) The stacking fault energy curves of $Al_{9.04}Co_{19.41}Cr_{20.77}Fe_{18.53}Ni_{32.23}$, $Fe_{27}Ni_{41}Co_{27}Al_5$, and pure Ni with FCC structure. FCC: Face-centered cubic.

DISCUSSION

Factors affecting the yield strength of composites with non-uniform structures

As described in Section 3.1, lamellar and core-shell models exhibit significant differences in mechanical behaviors during plastic deformation [Figure 2], and are strongly influenced by alloy composition. In this section, the yield strengths of all models are compared in detail. The main factors governing the yield strength are intrinsic physical characteristics at heterogeneous interfaces and the mechanical properties of single phases[38,39]. The yield strengths of three metallic models with different non-uniform structures, the atomic potential energy analysis at heterogeneous interfaces in lamellar models with different compositions, the engineering stress-strain curves of FCC and B2 single crystals under uniaxial tension, and the stacking fault energies of FCC single crystals with different compositions are shown in Figure 12A-D, respectively.

For models with identical composition but different structures, the yield strength of the lamellar model is significantly higher than that of the core-shell structure [Figure 12A]. The initial dislocation densities of the three models for $AlCoCrFeNi_{2.1}$ alloy are 13.58×10^{14}, 111.5×10^{14}, and 95.6×10^{14} m^{-2}, respectively. This indicates that the initial DD at the heterogeneous interface is much lower than that of the core-shell model. In other words, a higher stress is required to activate dislocation slip, resulting in a higher yield strength.

As the number of alloying elements decreases, the yield strength of the lamellar model increases significantly [Figure 12A]. Detailed analysis of atomic potential energy at heterogeneous interfaces in lamellar models

reveals that the number of low-potential-energy atoms increases with decreasing elemental diversity [Figure 12B], indicating that reduced interfacial potential energy strengthens interfacial stability. In addition, comparison of single-crystal mechanical behaviors shows that the yield strength of single phases follows the order: Ni > $Fe_{27}Ni_{41}Co_{27}Al_5$ > NiAl > $Al_{9.04}Co_{19.41}Cr_{20.77}Fe_{18.53}Ni_{32.23}$ [Figure 12C]. That is, the yield strength of FCC single crystals increases with decreasing alloying element species. Since the activated dislocations in the model are mainly SPDs, whose activation is closely related to unstable SFE, the SFEs of the three FCC single crystals were analyzed. The results show that the unstable SFE and the intrinsic SFE of Ni are the highest [Figure 12D], meaning the highest stress is required to activate SPD slip. The activation of dislocations leads to a decrease in stress. Thus, pure Ni exhibits the most significant stress fluctuations during deformation among all investigated single crystals. $Fe_{27}Ni_{41}Co_{27}Al_5$ and $Al_{9.04}Co_{19.41}Cr_{20.77}Fe_{18.53}Ni_{32.23}$ exhibit similar stacking fault energies, leading to small differences in yield strength. In summary, as the number of alloying elements decreases, the stability of heterogeneous interfaces, the yield strength of single crystals, and the SFE all increase, collectively enhancing the yield strength of lamellar models.

Differences in deformation mechanisms of composites with non-uniform structures

After entering plastic deformation, the characteristic mechanical behaviors of the composites depend on the activation of deformation systems and the dynamic evolution of micro-defects[36,41]. In this section, the dynamic evolutions of micro-deformation mechanisms were analyzed in detail. Since both twins and stacking faults are characterized by HCP atoms, and their formation both generates coherent interfaces that dynamically refine grains and hinder dislocation slip[55,56], the dynamic evolution of the HCP volume fraction was used to represent these two deformation configurations. The evolutions of micro-deformation configurations in the three-component alloy models with different non-uniform structures during deformation are shown in Figure 13. In the models with different compositions, a higher DD corresponds to a higher volume fraction of the HCP phase. However, the volume fraction of the HCP phase in all models is below 10%, indicating that the number of stacking faults and twins is limited and insufficient to induce significant work hardening in the later deformation stages. The B2-core models exhibit the highest DD, corresponding to the highest volume fraction of HCP atoms and a relatively low VSA [$Fe_{20}Co_{20}Ni_{41}Al_{19}$ (at.%) and Ni + NiAl]. This indicates that the activation of twinning and stacking faults is closely related to dislocation slip, and the coordinated deformation of dislocations, twins, and stacking faults inhibits void propagation, thereby promoting uniform deformation. In addition, the rapid propagation of voids in the lamellar and FCC-core models of $Fe_{20}Co_{20}Ni_{41}Al_{19}$ and Ni + NiAl is the main factor responsible for fracture. In summary, the limited number of activated twins and stacking faults in lamellar models readily leads to the concentration and rapid propagation of defects at heterogeneous interfaces, thereby deteriorating plasticity. For the core-shell models, when the phase with fewer deformation systems is located in the core, the plastic deformation capability of the metal can be optimized.

Effect of configurational entropy on plastic deformation mechanisms

As shown in Figure 13, the density of activated dislocations decreases significantly with decreasing alloying element species. To reveal the physical mechanism, the effects of lattice distortion (LD, induced by configurational entropy) and SFE on dislocation slip are thoroughly discussed in this section. According to the classical formula for configurational entropy: $\Delta S_{\mathrm{mix}} = -\mathrm{R}\sum_{i}^{n} c_i \ln c_i$. In this equation, c_i stands for the atomic percentage of the i-th element, R and n represent the gas constant and the total number of components, respectively[57,58]. Due to differences in the atomic radii of alloying elements, $Al_{9.04}Co_{19.41}Cr_{20.77}Fe_{18.53}Ni_{32.23}$, $Fe_{27}Ni_{41}Co_{27}Al_{5,}$ and pure Ni exhibit different degrees of LD. LD is usually quantified by the difference in atomic size δ, which is expressed as[58-60]:

$$\delta = 100\sqrt{\sum_{i}^{n} c_i \left(1 - \frac{r_i}{\bar{r}}\right)^2} \tag{1}$$

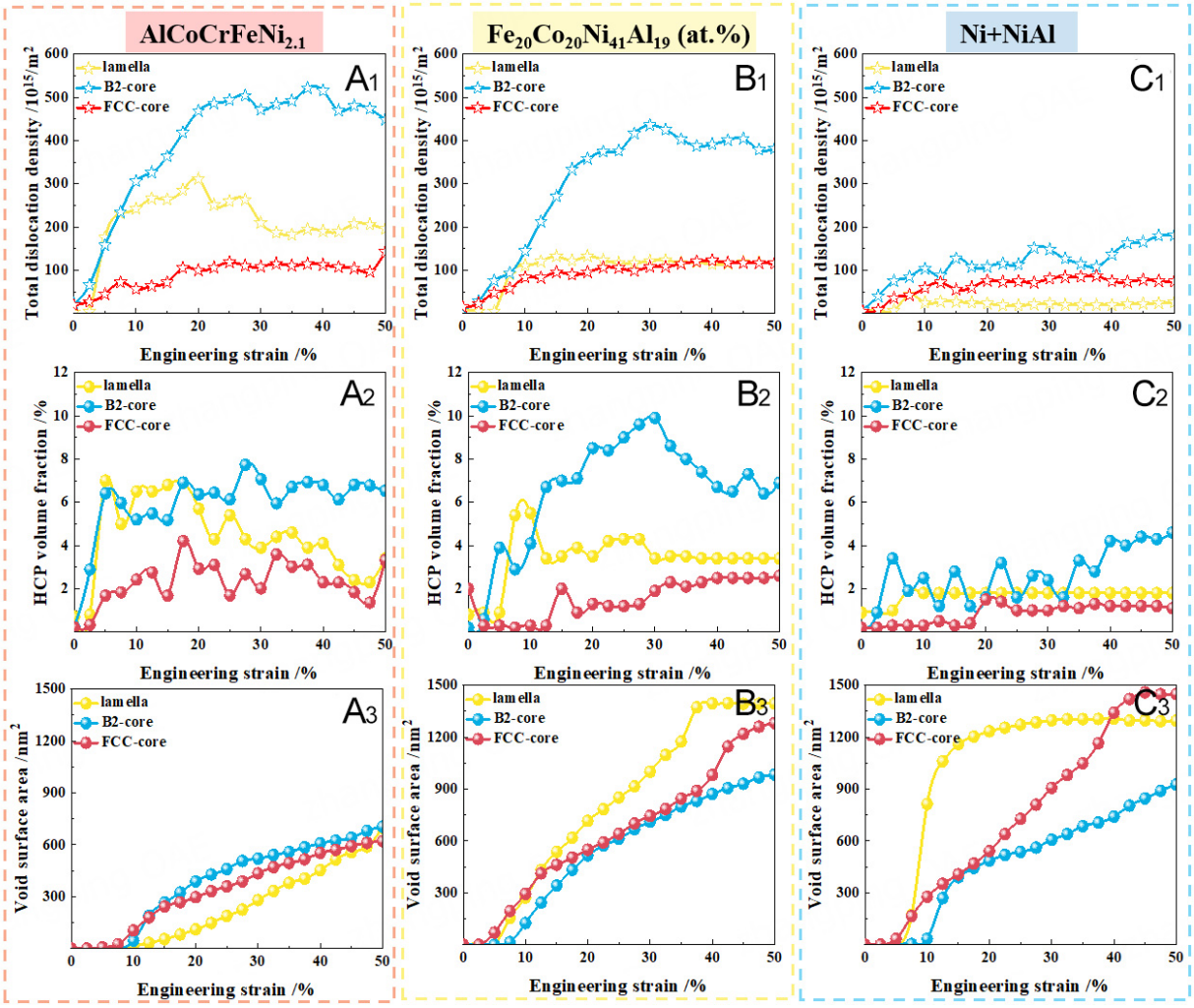


Figure 13. Evolutions of micro-deformation configurations in three alloy models with different compositions and non-uniform structures. (A_1-C_1) Dislocation density; (A_2-C_2) Volume fraction of HCP atoms; (A_3-C_3) Void surface area. FCC: Face-centered cubic; HCP: hexagonal close-packed.

$$\bar{r} = \sum_{i}^{n} c_i r_i \tag{2}$$

Here, n denotes the element species, $\bar{r}$ represents the average atomic radius, and c_i and r_i correspond to the atomic percentage and atomic radius of the i-th element, respectively. Accordingly, the configurational entropies of $Al_{9.04}Co_{19.41}Cr_{20.77}Fe_{18.53}Ni_{32.23}$, $Fe_{27}Ni_{41}Co_{27}Al_5$, and Ni are 1.54, 1.22, and 0 R, respectively. The LDs are 4.24, 3.28, and 0, respectively. Figure 14 shows the atomic structures of the FCC phases with different compositions. Their atomic arrangement further indicates that the degree of disorder decreases as the number of alloying elements decreases, i.e., both the configurational entropy and LD decrease. Therefore, lower configurational entropy leads to lower LD, which further reduces DD. This is consistent with MD simulation results of the deformation behaviors for CoCrNi-based medium-entropy alloys (MEAs)[61-63]. Furthermore, compared with $Al_{9.04}Co_{19.41}Cr_{20.77}Fe_{18.53}Ni_{32.23}$ and $Fe_{27}Ni_{41}Co_{27}Al_5$, pure Ni exhibits a significantly higher SFE [Figure 12D], making SPDs more difficult to activate, which is another key factor responsible for the poor plastic deformation capability of the Ni + NiAl model. In summary, Chemical composition exerts direct impacts on configurational entropy, LD, and SFE. Notably, configurational entropy shows a positive correlation with LD. LD and SFE jointly dominate the activation of SPDs. While the nucleation of twins and SFs depends primarily on SFE, the dislocation storage capacity of the alloy is predominantly governed by LD.

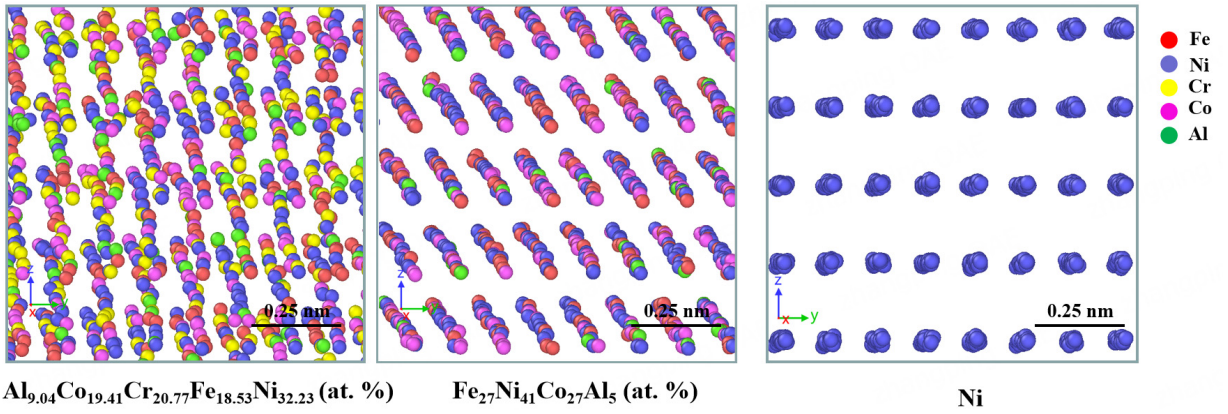


Figure 14. Atomic structures of $Al_{9.04}Co_{19.41}Cr_{20.77}Fe_{18.53}Ni_{32.23}$, $Fe_{27}Ni_{41}Co_{27}Al_5$, and pure Ni with FCC structure. FCC: Face-centered cubic.

CONCLUSION

In this work, MD simulations were performed to investigate the mechanical behaviors and deformation mechanisms of FCC/B2 composites with lamellar and core-shell structures in $AlCoCrFeNi_{2.1}$, $Fe_{20}Co_{20}Ni_{41}Al_{19}$ (at.%), and Ni + NiAl alloys under uniaxial tensile deformation. By further examining the deformation processes of composites with different compositions, the effects of configurational entropy, LD, and SFE on micro-deformation mechanisms were clarified. This study investigates a simplified FCC/NiAl composite model and appropriately qualifies the extent to which the findings can be generalized to real multicomponent alloys. The main conclusions are as follows.

(1) During the elastic deformation stage, the elastic modulus of all FCC/B2 composites is nearly identical. After plastic deformation occurs, the lamellar model exhibits higher yield strength but inferior plasticity compared with the core-shell structure. For alloys with different compositions, the yield strength of the lamellar model increases significantly with decreasing alloying element species, whereas the yield strength of the core-shell models is less affected.

(2) Among the three alloy systems, the B2-core model exhibits excellent plastic deformation capability, which originates from the cooperative deformation of abundant dislocations, twins, and stacking faults that effectively suppress the propagation of voids. In contrast, fewer deformation systems are activated in the lamellar models of Ni + NiAl alloys, leading to the formation and rapid propagation of voids and consequently poor plasticity.

(3) With decreasing configurational entropy, the increase in strength for lamellar models is attributed to the improved stability of heterogeneous interfaces and the increased yield strength and SFE of the FCC phase. Compared with MEAs, the FCC phase in the Ni + NiAl model exhibits lower LD, which reduces dislocation storage capacity. Meanwhile, the high SFE of pure Ni hinders SPD activation. These factors reduce the number of activated deformation systems in the lamellar model of Ni + NiAl alloy, resulting in inferior plastic deformation capacity.

DECLARATIONS

Authors' contributions

Conceived and designed the study, drafted the manuscript: Zhang, H.; Jia, N.
Provided valuable suggestions: Wang, M.; Zheng, A.; Ji, H.
All authors reviewed and edited the final version.

Availability of data and materials

The original contributions presented in this study are included in the article. Further inquiries can be

directed to the corresponding authors.

AI and AI-assisted tools statement

Not applicable.

Financial support and sponsorship

This work was supported by the Natural Science Foundation of Hebei Province (E2024209052), the Outstanding Young Talent Project of Hebei Provincial Education Department (BJ2026031), and the Youth Scholars Promotion Plan of North China University of Science and Technology (QNTJ202307).

Conflicts of interest

All authors declared no conflicts of interest.

Ethical approval and consent to participate

Not applicable.

Consent for publication

Not applicable.

Copyright

© The Author(s) 2026.

REFERENCES

1. Zhu, Y.; Wu, X. Heterostructured materials. *Prog. Mater. Sci.* **2023**, *131*, 101019. DOI
2. Sun, J.; An, X. Hierarchical heterogeneities engineering towards sustainable high-performing alloys. *Mater. Today. Sustain.* **2024**, *25*, 100694. DOI
3. Zhang, X. Heterostructures: new opportunities for functional materials. *Mater. Res. Lett.* **2020**, *8*, 49-59. DOI
4. Wu, X.; Jiang, P.; Chen, L.; Yuan, F.; Zhu, Y. T. Extraordinary strain hardening by gradient structure. *Proc. Natl. Acad. Sci. U. S. A.* **2014**, *111*, 7197-201. DOI PubMed PMC
5. Pan, Q.; Zhang, L.; Feng, R.; et al. Gradient cell-structured high-entropy alloy with exceptional strength and ductility. *Science* **2021**, *374*, 984-9. DOI
6. Xu, X.; Li, X.; Gou, X.; Li, Y.; Ye, Q.; Tian, Y. Synergistic enhancement of strength, ductility, and toughness in a low carbon micro-alloy steel with an ultrafine-grained heterogeneous lamellar structure. *Mater. Sci. Eng. A.* **2023**, *878*, 145205. DOI
7. Wu, X.; Yang, M.; Yuan, F.; et al. Heterogeneous lamella structure unites ultrafine-grain strength with coarse-grain ductility. *Proc. Natl. Acad. Sci. U. S. A.* **2015**, *112*, 14501-5. DOI PubMed PMC
8. Li, G.; Jiang, J.; Ma, H.; et al. Superior strength-ductility synergy in three-dimensional heterogeneous-nanostructured metals. *Acta. Mater.* **2023**, *256*, 119143. DOI
9. Gu, L.; Meng, A.; Chen, X.; Zhao, Y. Simultaneously enhancing strength and ductility of HCP titanium via multi-modal grain induced extra <c+a> dislocation hardening. *Acta. Mater.* **2023**, *252*, 118949. DOI
10. Zhu, Z.; Nguyen, Q.; Ng, F.; et al. Hierarchical microstructure and strengthening mechanisms of a CoCrFeNiMn high entropy alloy additively manufactured by selective laser melting. *Scr. Mater.* **2018**, *154*, 20-4. DOI
11. Zhu, Z. G.; An, X. H.; Lu, W. J.; et al. Selective laser melting enabling the hierarchically heterogeneous microstructure and excellent mechanical properties in an interstitial solute strengthened high entropy alloy. *Mater. Res. Lett.* **2019**, *7*, 453-9. DOI
12. Li, J.; Lu, W.; Chen, S.; Liu, C. Revealing extra strengthening and strain hardening in heterogeneous two-phase nanostructures. *Int. J. Plast.* **2020**, *126*, 102626. DOI
13. Huang, J.; Liu, Y.; Xu, T.; et al. Dual-phase hetero-structured strategy to improve ductility of a low carbon martensitic steel. *Mater. Sci. Eng. A.* **2022**, *834*, 142584. DOI
14. Wu, X.; Zhu, Y.; Lu, K. Ductility and strain hardening in gradient and lamellar structured materials. *Scr. Mater.* **2020**, *186*, 321-5. DOI
15. Sun, Y.; Kong, X.; Wang, Z. Superior mechanical properties and deformation mechanisms of a 304 stainless steel plate with gradient nanostructure. *Int. J. Plast.* **2022**, *155*, 103336. DOI
16. Zhu, Y. Creating multifunctionality with hierarchical heterostructures. *Mater. Res. Lett.* **2025**, *13*, 175-8. DOI
17. Zhu, Y.; Ameyama, K.; Anderson, P. M.; et al. Heterostructured materials: superior properties from hetero-zone interaction. *Mater. Res. Lett.* **2021**, *9*, 1-31. DOI

18. Dong, X.; Gao, B.; Xiao, L.; et al. Heterostructured metallic structural materials: research methods, properties, and future perspectives. *Adv. Funct. Mater.* **2024**, *34*, 2410521. DOI
19. Wang, Z.; Bai, X.; Wang, J.; et al. Revisiting the development of eutectic high-entropy alloys over the past decade (2014-2024): design, manufacturing, and applications. *Acta. Metall. Sin.* **2025**, *61*, 1-11. DOI
20. Sathiyamoorthi, P.; Kim, H. S. High-entropy alloys with heterogeneous microstructure: Processing and mechanical properties. *Prog. Mater. Sci.* **2022**, *123*, 100709. DOI
21. Shi, P.; Li, R.; Li, Y.; et al. Hierarchical crack buffering triples ductility in eutectic herringbone high-entropy alloys. *Science* **2021**, *373*, 912-8. DOI
22. Lu, Y.; Dong, Y.; Guo, S.; et al. A promising new class of high-temperature alloys: eutectic high-entropy alloys. *Sci. Rep.* **2014**, *4*, 6200. DOI PubMed PMC
23. Lu, Y.; Dong, Y.; Jiang, H.; et al. Promising properties and future trend of eutectic high entropy alloys. *Scr. Mater.* **2020**, *187*, 202-9. DOI
24. Ren, J.; Zhang, Y.; Zhao, D.; et al. Strong yet ductile nanolamellar high-entropy alloys by additive manufacturing. *Nature* **2022**, *608*, 62-8. DOI
25. Shi, P.; Ren, W.; Zheng, T.; et al. Enhanced strength-ductility synergy in ultrafine-grained eutectic high-entropy alloys by inheriting microstructural lamellae. *Nat. Commun.* **2019**, *10*, 489. DOI
26. Shi, P.; Zhong, Y.; Li, Y.; et al. Multistage work hardening assisted by multi-type twinning in ultrafine-grained heterostructural eutectic high-entropy alloys. *Mater. Today.* **2020**, *41*, 62-71. DOI
27. Shi, P.; Li, Y.; Jiang, X.; et al. Strong-yet-ductile eutectic alloys employing cocoon-like nanometer-sized dislocation cells. *Adv. Mater.* **2024**, *36*, e2405459. DOI
28. Wang, L.; Lu, W.; Wang, X.; et al. Grain-boundary precipitation architected hard-shell heterostructure achieves extraordinary strain hardening in high-entropy alloys. *Acta. Mater.* **2026**, *310*, 122151. DOI
29. Zhang, Q.; Chen, Z.; Dong, Y.; Li, C.; Wang, Y. High strength and ductility eutectic high entropy alloy with unique core-shell structure. *J. Alloys. Compd.* **2024**, *976*, 173141. DOI
30. Kim, R. E.; Lee, J. H.; Haftlang, F.; et al. Hierarchical ferrous medium entropy with heterogeneous precipitates embedded in core-shell grain structure for superior mechanical properties. *Acta. Mater.* **2024**, *281*, 120397. DOI
31. Fang, X.; He, G.; Zheng, C.; et al. Effect of heterostructure and hetero-deformation induced hardening on the strength and ductility of brass. *Acta. Mater.* **2020**, *186*, 644-55. DOI
32. Yang, Y.; Liu, Y.; Jiang, S.; et al. Achieving exceptional strength and ductility combination in a heterostructured Mg-Y alloy with densely refined twins. *J. Mater. Sci. Technol.* **2024**, *189*, 132-45. DOI
33. Jiang, S.; Peng, R. L.; He, Z.; et al. Mechanical behavior anisotropy of multilayered metallic composites revealed by in-situ synchrotron X-ray diffraction: example of Ti/Nb laminates processed by accumulative roll bonding. *Acta. Mater.* **2025**, *287*, 120815. DOI
34. Pang, J.; Xiong, T.; Yang, W.; et al. Atomic scale structure dominated FCC and B2 responses to He ion irradiation in eutectic high-entropy alloy $AlCoCrFeNi_{2.1}$. *J. Mater. Sci. Technol.* **2022**, *129*, 87-95. DOI
35. Lu, Y.; Wu, X.; Fu, Z.; et al. Ductile and ultrahigh-strength eutectic high-entropy alloys by large-volume 3D printing. *J. Mater. Sci. Technol.* **2022**, *126*, 15-21. DOI
36. Choudhuri, D.; Campbell, A. Interface dominated deformation mechanisms in two-phase *fcc*/B2 nanostructures: Nishiyama-Wasserman vs. Kurdjumov-Sachs interfaces. *Comput. Mater. Sci.* **2020**, *177*, 109577. DOI
37. Ji, W.; Gao, S.; Jarlöv, A.; et al. Designing maximal strength in nanolamellar eutectic high-entropy alloys. *Adv. Mater.* **2025**, *37*, e2500149. DOI
38. Yang, J.; Zhang, H.; Ji, H.; Jia, N. Molecular dynamics simulations of micromechanical behaviours for $AlCoCrFeNi_{2.1}$ high entropy alloy during nanoindentation. *Acta. Metall. Sin.* **2025**, *38*, 218-32. DOI
39. Zhang, H.; He, Z.; Zhang, M.; Jiang, S.; Jia, N.; Feng, Y. Orientation-dependent micromechanical behaviours of FCC/B2 dualphase $AlCoCrFeNi_{2.1}$ high entropy nanopillars studied by atomic simulations. *Mater. Today. Commun.* **2025**, *48*, 113648. DOI
40. Bian, J.; Yuan, W.; Ni, N.; Shao, Z.; Wang, G. Tunable mechanical properties of high-entropy alloy nanoparticles with core-shell structure. *Mater. Today. Commun.* **2025**, *49*, 113839. DOI
41. Choudhuri, D.; Srinivasan, S. G.; Mishra, R. S. Deformation of lamellar FCC-B2 nanostructures containing Kurdjumov-Sachs interfaces: relation between interfacial structure and plasticity. *Int. J. Plast.* **2020**, *125*, 191-209. DOI
42. Plimpton, S. Fast parallel algorithms for short-range molecular dynamics. *J. Comput. Phys.* **1995**, *117*, 1-19. DOI
43. Farkas, D.; Caro, A. Model interatomic potentials for Fe-Ni-Cr-Co-Al high-entropy alloys. *J. Mater. Res.* **2020**, *35*, 3031-40. DOI
44. Lin, K.; Tao, P.; Liu, R.; Huang, Z.; Xiong, Z. Effect of crystallographic orientation on mechanical properties of $Al_{0.25}CoCrFeNi$ high entropy alloy under tension. *Mater. Today. Commun.* **2024**, *41*, 110306. DOI

45. Liu, X.; Yan, J. Atomistic simulations of tensile properties and deformation mechanisms in a gradient nanostructured $Al_{0.3}$CrFeCoNi high-entropy alloy. *Appl. Phys. A.* **2024**, *130*, 7855. DOI
46. Ren, J.; Gui, Y.; Gao, Q.; et al. Mechanical response and plastic deformation in single- and dual-phase polycrystalline FeNiAl alloys: molecular dynamics analysis. *J. Mater. Sci.* **2024**, *59*, 14405-19. DOI
47. Yoon, S.; Kimura, Y.; Uchida, M.; Ju, Y.; Toku, Y. High temperature tensile and compressive behaviors of nanostructured polycrystalline AlCoCrFeNi high entropy alloy: a molecular dynamics study. *J. Eng. Mater. Technol.* **2024**, *146*, 021003. DOI
48. Choudhuri, D.; Banerjee, R.; Srinivasan, S. G. Uniaxial deformation of face-centered-cubic(Ni)-ordered B2(NiAl) bicrystals: atomistic mechanisms near a Kurdjumov-Sachs interface. *J. Mater. Sci.* **2018**, *53*, 5684-95. DOI
49. Stukowski, A. Visualization and analysis of atomistic simulation data with OVITO-the open visualization tool. *Model. Simul. Mater. Sci. Eng.* **2010**, *18*, 015012. DOI
50. Stukowski, A.; Bulatov, V. V.; Arsenlis, A. Automated identification and indexing of dislocations in crystal interfaces. *Model. Simul. Mater. Sci. Eng.* **2012**, *20*, 085007. DOI
51. Stukowski, A. Structure identification methods for atomistic simulations of crystalline materials. *Model. Simul. Mater. Sci. Eng.* **2012**, *20*, 045021. DOI
52. Krone, M.; Stone, J. E.; Ertl, T.; Schulten, K. Fast visualization of gaussian density surfaces for molecular dynamics and particle system trajectories. In *Eurographics Conference on Visualization (EuroVis)*, Vienna, Austria; 2012. DOI
53. Yang, X.; Zhou, K.; Han, X.; et al. A Study on the mechanical properties of Ni-Al alloy based on molecular dynamics simulation. *Coatings* **2026**, *16*, 168. DOI
54. Huang, C.; Wang, Y.; Ma, X.; et al. Interface affected zone for optimal strength and ductility in heterogeneous laminate. *Mater. Today.* **2018**, *21*, 713-9. DOI
55. Sun, J.; Li, H.; Chen, Y.; An, X. Bidirectional phase transformations in multi-principal element alloys: mechanisms, physics, and mechanical property implications. *Adv. Sci.* **2024**, *11*, e2407283. DOI
56. Wu, H.; Fan, G. An overview of tailoring strain delocalization for strength-ductility synergy. *Prog. Mater. Sci.* **2020**, *113*, 100675. DOI
57. Zhang, Y.; Zuo, T. T.; Tang, Z.; et al. Microstructures and properties of high-entropy alloys. *Prog. Mater. Sci.* **2014**, *61*, 1-93. DOI
58. Zhang, W.; Liaw, P. K.; Zhang, Y. Science and technology in high-entropy alloys. *Sci. China. Mater.* **2018**, *61*, 2-22. DOI
59. Xu, B.; Huang, S.; Lu, W.; et al. Crossover from sluggish to accelerated diffusion in multi-principal element alloys induced by lattice distortion. *Acta. Mater.* **2026**, *316*, 122431. DOI
60. Ghadami, F.; Davoudabadi, M. A. Si-induced lattice distortion and its role in enhancing the tribological performance of APS AlCoCrFeNiSi_x ($0.1 \leq x \leq 0.5$) high-entropy alloy coatings. *Surf. Coat. Technol.* **2026**, *530*, 133551. DOI
61. Huang, G.; Zhang, X.; Zou, X.; et al. Roles of lattice distortion and chemical short-range order in dislocation drag and strain-rate sensitivity over wide strain rates. *J. Mech. Phys. Solids.* **2026**, *215*, 106723. DOI
62. Meng, Y.; Zeng, X.; Liu, S.; et al. Effect of lattice distortion and chemical short-range order on the phase transformation behavior of high entropy alloys under high strain rates. *Int. J. Plast.* **2026**, *197*, 104584. DOI
63. Wang, L.; Liu, B.; Zhou, J.; Cao, Y.; Zhang, F.; Zhao, Y. Unconventional dislocation starvation behavior of medium-entropy alloy single crystal pillars containing pre-existing dislocations. *J. Mater. Sci. Technol.* **2023**, *142*, 60-75. DOI

Disclaimer/Publisher's Note: All statements, opinions, and data contained in this publication are solely those of the individual author(s) and contributor(s) and do not necessarily reflect those of OAE and/or the editor(s). OAE and/or the editor(s) disclaim any responsibility for harm to persons or property resulting from the use of any ideas, methods, instructions, or products mentioned in the content.

© The Author(s) 2026. Open Access This article is licensed under a Creative Commons Attribution 4.0 International License (https://creativecommons.org/licenses/by/4.0/), which permits unrestricted use, sharing, adaptation, distribution and reproduction in any medium or format, for any purpose, even commercially, as long as you give appropriate credit to the original author(s) and the source, provide a link to the Creative Commons license, and indicate if changes were made.